



# Deep machine learning for cell segmentation and quantitative analysis of radial plant growth

Alexandra Zakieva <sup>a</sup>, Lorenzo Cerrone <sup>b</sup>, Thomas Greb <sup>a,\*</sup>

<sup>a</sup> Centre for Organismal Studies (COS), Heidelberg University, Heidelberg, Germany

<sup>b</sup> Interdisciplinary Center for Scientific Computing (IWR), Heidelberg University, Heidelberg, Germany

## ARTICLE INFO

**Keywords:**

Cambium  
Radial plant growth  
Wood formation  
PlantSeg  
Automated image analysis  
Quantitative histology  
Arabidopsis hypocotyl

## ABSTRACT

Plants produce the major part of terrestrial biomass and are long-term deposits of atmospheric carbon. This capacity is to a large extent due to radial growth of woody species – a process driven by cambium stem cells located in distinct niches of shoot and root axes. In the model species *Arabidopsis thaliana*, thousands of cells are produced by the cambium in radial orientation generating a complex organ anatomy enabling long-distance transport, mechanical support and protection against biotic and abiotic stressors. These complex organ dynamics make a comprehensive and unbiased analysis of radial growth challenging and asks for tools for automated quantification. Here, we combined the recently developed PlantSeg and MorphographX image analysis tools, to characterize tissue morphogenesis of the *Arabidopsis* hypocotyl. After sequential training of segmentation models on ovules, shoot apical meristems and adult hypocotyls using deep machine learning, followed by the training of cell type classification models, our pipeline segments complex images of transverse hypocotyl sections with high accuracy and classifies central hypocotyl cell types. By applying our pipeline on both wild type and *phloem intercalated with xylem* (*pxy*) mutants, we also show that this strategy faithfully detects major anatomical aberrations. Collectively, we conclude that our established pipeline is a powerful phenotyping tool comprehensively extracting cellular parameters and providing access to tissue topology during radial plant growth.

## 1. Introduction

Thickening of plant stems and roots by radial growth and, in extreme cases, their transformation into trunks in tree species, allows plants to build large bodies. In addition to ensuring mechanical support of those bodies, radial growth generates vascular tissues allowing transport of water, nutrients, sugars, and signaling molecules over long distances. The process of radial growth is based on stem cell activity in the cambium, a bifacial stem cell niche producing the water- and nutrient-transporting xylem (“wood”) usually toward the organ center and the sugar-transporting phloem toward the organ periphery (Fig. 1) (Haas et al., 2022; Greb and Lohmann, 2016). The resulting tissue morphology can vary across species and present evolutionary adaptations to distinct ecological niches (Spicer and Groover, 2010). Importantly, although radial plant growth is a major source of durable biomass, an essential carbon sink, and harbors central ecological relevance, the quantitative analysis of its anatomy and dynamics is hampered by obstacles for direct imaging and by the lack of systematic analysis tools.

For investigating complex morphogenetic processes like radial plant growth, it is essential to comprehensively quantify cell numbers and shapes. Recently, novel computational methods were developed to realize this quantification on complex microscope images. These methods allow efficient automated segmentation of image data from tissues into single cells and determination of their morphological descriptors. An unbiased quantitative analysis of cell morphology and tissue topology becomes thus possible. This approach, called quantitative histology, is critical to perform statistically solid phenotyping of samples hard to characterize by classical qualitative or semi-quantitative means. In recent studies (Strauss et al., 2022; Berg et al., 2019), segmentation and classification models not only integrated image information but also image interpretation by human specialists through trained Convolutional Neural Networks (CNNs). In these cases, generating ground truth, which are manually corrected segmentations, for training CNN-dependent models is usually the most time-consuming step.

In the past, CNNs were applied on 3D confocal images of the

\* Corresponding author at: Centre for Organismal Studies (COS), Heidelberg University, Im Neuenheimer Feld 360, 69120 Heidelberg, Germany.  
E-mail address: [thomas.greb@cos.uni-heidelberg.de](mailto:thomas.greb@cos.uni-heidelberg.de) (T. Greb).

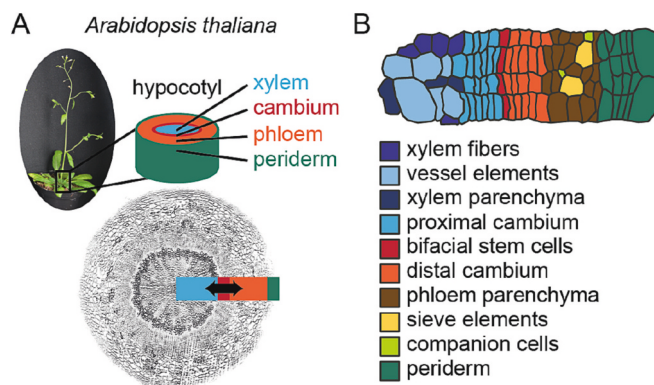


**Fig. 1.** Anatomy and cell type composition of the *Arabidopsis* hypocotyl. (A) Radial growth and hypocotyl tissues. On the bottom, a hypocotyl transversal section. The double-arrow indicates bidirectional tissue production by cambium stem cells. (B) Detailed view on hypocotyl cell types.

*Arabidopsis* shoot apical meristem (SAM), lateral root primordia (LRP) and ovules with stained cell walls employing the “PlantSeg” pipeline (Wolny et al., 2020). After boundary prediction with trained CNNs, PlantSeg supports different graph partitioning algorithms like Watershed, MultiCut, or MutexWS transforming a pixelized boundary prediction map into a superpixelled segmentation where every superpixel corresponds to a label or a cell (Wolny et al., 2020). However, although being versatile when being applied on 3D image data, the PlantSeg pipeline has not yet been applied on less voluminous 2D data which are not necessarily less challenging for automated image analysis with regard to signal noise and cellular heterogeneity.

In this study, we used radial plant growth of *Arabidopsis thaliana* as a case study for applying PlantSeg on 2D representations of organs containing highly heterogeneous tissues and several thousands of cells. In particular, we analyzed the hypocotyl which is the organ connecting shoot and root systems and shows the highest degree of radial organ growth in this species (Lehmann and Hardtke, 2016). As the hypocotyl grows exclusively radially in adult plants (Fig. 1), transversal sections are sufficient to visualize its dynamics in a first approximation and, thus, is ideal for a 2D-based automated quantitative analysis. In general, images from hypocotyl sections are challenging samples to segment and previous image analysis studies were usually limited to vascular tissues, included cumbersome manual cell boundary annotation or required extensive computing time (Bagdassarian et al., 2020; Sankar et al., 2014). In addition, the power of automated image analyses is usually neither trained nor tested on samples with altered anatomical properties (Hall et al., 2016). Here, by generating trained CNN U-net models, we enable application of the PlantSeg pipeline in the context of radial plant growth and establish this tool for automated anatomical analyses.

## 2. Materials and methods

### 2.1. Plant material and growth conditions

*Arabidopsis thaliana* of Columbia-0 ecotype was used throughout this whole study. phloem intercalated with xylem-2 (pxy-2) (SALK\_108191) and pxy-4 (SALK\_009542) T-DNA insertion lines were provided by Nottingham *Arabidopsis* Stock Centre and genotyped as previously described (Fisher and Turner, 2007). Seeds were surface sterilized using 70 % v/v EtOH 0.1 % v/v Triton X-100 for 10 min and washed with 95 % v/v EtOH for five minutes. Then, excess of ethanol was removed, and seeds were dried in a sterile hood. Sterilized seeds were then sown in Petri dishes with autoclaved medium (½ MS 0.5 g/L MES 10 g/L sucrose 8 g/L Phytoagar pH 5.8). The Petri dishes with seeds were then stratified in darkness at 4 °C for at least three days. Seeds were transferred to soil after stratification. Seedlings were grown on soil in short-day conditions

(10 h light and 14 h darkness) for 21 days and then moved to long-day conditions (16 h light and 8 h darkness).

### 2.2. Histological imaging

Plants were collected from soil and washed in tap water to get access to hypocotyls. Hypocotyls were collected with a scalpel and fixed in 500 µL of 4 % w/v PFA dissolved in PBS pH 7.0 in darkness at 4 °C overnight. Then, hypocotyls were incubated for 20 min in 10 % sucrose, 1 % w/v PFA dissolved in PBS pH 7.0 then, for 20 min in the same solution but with 20 % sucrose, and for 30 min in the same solution but with 30 % sucrose. Afterwards, hypocotyls were embedded in 7 % low temperature-melting agarose and sectioned transversally to the longitudinal axis using a Leica VT1000 S vibratome carrying Wilcoxon blades (one blade each for three samples) at the speed set to 10 units and the frequency set to 70 Hz. Hypocotyls were immersed in PBS pH 7.0 buffer and progressively cut following the stem to root direction. After the two first sections, four sections of 75 µm thickness were collected with a fine brush into 500 µL of ClearSee (10 % w/v xylitol, 15 % w/v sodium deoxycholate, 25 % w/v urea). Afterwards, the samples were cleared and stained as described previously (Ursache et al., 2018) with modifications. Hypocotyl sections were first stained overnight with 0.2 % w/v Basic Fuchsin (#B0904, Sigma-Aldrich, St. Louis, US) diluted in ClearSee. After washing three times with ClearSee, sections were stained with 0.1 % w/v DirectYellow96 (#S472409, Sigma-Aldrich, St. Louis, US) diluted in ClearSee, washed three times with ClearSee and mounted in ClearSee on microscope slides. Hypocotyl sections were imaged using a Leica SP8 confocal microscope using a 20x glycerol-immersed objective. Signals for the different fluorescence channels were acquired sequentially. DirectYellow96 was excited at 488 nm, its emission was collected using a 500–540 nm band-pass filter and Basic Fuchsin was excited at 561 nm, its emission was collected using a 600–650 nm band-pass filter. Transmission light images were acquired in parallel to assess the transparency of samples. Imaging was realized with bidirectional scan direction X, 1.5 AU pinhole, 3 times line averaging, at 2048 × 2048 image resolution, 400 Hz scan speed.

### 2.3. Image and data analysis

The acquired images were processed in FIJI (Schindelin et al., 2012). One section out of four per plant with the lowest amount of imaging artefacts was selected, and a quarter of the hypocotyl section was cropped and analyzed by quantitative histology. The images produced when collecting the DirectYellow96 channel were processed in PlantSeg according to published documentation (<https://github.com/hci-unihd/plant-seg>). The tile scans of hypocotyl images were processed in FIJI (Macro 2, available at <https://github.com/thomasgreib/Zakieva-et-al-hypoQuant.git>). Ground truth was generated using the proofreading tool of PlantSeg according to published documentation (<https://github.com/hci-unihd/plant-seg-tools>). More specifically, the images were submitted to a CNN U-net model for cell boundary prediction previously trained on three-dimensional (3D) confocal images of *Arabidopsis* ovules and additionally trained with 3D confocal images of SAMs (Wolny et al., 2020). 25 ground truth images in total of wild type, pxy-2 and pxy-4 at 3, 4, 4.5 and 5 weeks post-germination (wpg) were used for the training of a CNN U-net two-dimensional (2D) boundary prediction model. Overall, we did two rounds of training using ground truth consisting of corrected segmentations from ten sections each and an additional last training round using ground truth consisting of corrected segmentations from five sections. The PlantSeg parameters were set as follows: prediction patch size – 1 × 128 × 128, stride – Accurate, segmentation algorithm – MutexWS, under-/over-segmentation factors – 0.45, CNN prediction threshold – 0.06, Watershed seeds sigma – 4.2, Watershed boundary sigma – 4.2. The performance of segmentation parameter settings and boundary prediction models was evaluated according to published documentation (<https://github.com/hci-unihd/pla>

[nt-seg/tree/master/evaluation](#)). The segmentation scores obtained from this evaluation (Supplementary Data – Supplementary Table 1) were processed in R (<https://www.R-project.org>). After processing in PlantSeg, the resulting segmentations and raw confocal images were submitted to MGX (Strauss et al., 2022). A vectorized cell mesh was generated from the superpixel segmentation. The original confocal images, proofread segmentations and cell meshes are available as Supplementary Data. Basic Fuchsin and DirectYellow96 confocal images were projected on the mesh. 15 cell descriptors were computed as described previously (Montenegro-Johnson et al., 2019; Wunderling et al., 2017; Jackson et al., 2017; Sapala et al., 2018): 1: Basic Fuchsin signal, 2: DirectYellow96 signal, 3: area, 4: perimeter, 5: major axis, 6: minor axis, 7: aspect ratio, 8: circularity, 9: rectangularity, 10: lobeyness, 11: incline angle, 12: cell degree, 13: betweenness centrality, 14: radial coordinate, 15: circumferential coordinate. Cell type classification was realized as described previously (Sankar et al., 2014). The resulting data were extracted as .csv files (Supplementary Data – Supplementary Table 2) and processed in R.

### 3. Results

#### 3.1. pxy mutants show an altered hypocotyl anatomy

To generate material for an automated anatomical analysis of radial plant growth, we collected *Arabidopsis* hypocotyls from three to five weeks after germination (3.5, 4, 4.5 and 5 weeks post germination, wpg) which is a phase of pronounced radial organ expansion (Fig. 2A-D). We co-stained hypocotyl sections by DirectYellow96 to highlight cell boundaries together with Basic Fuchsin to identify lignified and suberized cells by confocal imaging (Ursache et al., 2018). We harvested hypocotyls not only from wild type but also from two *pxy* mutant alleles (*pxy-2*, *pxy-4*) which show a considerable change in tissue anatomy (Etchells et al., 2012; Lebovka et al., 2023) with the purpose of training boundary prediction models not only on standard conditions but also on disturbed anatomies.

During the investigated time frame, hypocotyls at least doubled their diameter and xylem vessels marked by highly lignified walls were continuously produced by the cambium toward the hypocotyl centre (Fig. 2A-D). In addition, phloem sieve elements and companion cells formed phloem poles which could be identified based on their smaller cell size and agglomeration in groups (Fig. 2D). The initial cortex and epidermis detached at around 4 wpg (Fig. 2B) providing space for periderm growth, a secondary protective tissue layer producing bark in woody species (Serra et al., 2022). Within the periderm, the phellem is the outermost suberized tissue which, as expected, was marked by Basic Fuchsin staining (Fig. 2D, L, T). The phellem is produced by the phellogen, the proliferating stem cell area of the periderm which, in addition, produces the phelloidem toward the hypocotyl centre (Fig. 2F) (Serra et al., 2022). Naturally, cambium-derived phloem and phellogen-derived phelloidem meet at the inner border of the periderm (Fig. 1B). The phloem-periderm border can be identified as it is marked by a maximum in cell size and a slight change in cell morphology when moving along the radial axis of the hypocotyl section (Fig. 2G). At 4.5 wpg, previously described (Wunderling et al., 2018) tissue gaps at the phloem periphery appeared (Fig. 2C, D), presumably due to dilatation of these tissues by more proximal cambium-driven tissue production. At this developmental stage, also phloem fibers started to appear, visible due to their characteristic lignified cell walls (Fig. 2H, P, X).

In contrast to wild type, *pxy* mutants did, as previously described (Lebovka et al., 2023), not develop a clear ring-shaped cambium domain (Fig. 2L, T). In addition, distances between xylem vessels were larger in *pxy* mutants than in wild type and the xylem occupied more space in relation to peripheral tissues (Fig. 2D, L, T, O, W). Additionally to the previously described disorganized xylem (Fisher and Turner, 2007 (Fig. 2E, M, N, U, V)), the phloem was more disorganized in *pxy* mutants after 4 wpg (Fig. 2G, O, W). Moreover, the periderm appeared larger in

*pxy* mutants compared to wild type (Fig. 2D, L, T). Importantly, no qualitative difference comparing *pxy-2* to *pxy-4* was observed.

#### 3.2. Model training improved segmentation and boundary prediction

To initiate automated analysis, obtained images were next segmented using PlantSeg (Wolny et al., 2020) and manually corrected using the proofreading tool integrated into the PlantSeg platform. The resulting 25 ground truth images (Fig. 3A, B) were used for training of a CNN U-net model in three iterations. 10 ground truth images were used for the first, 10 for the second and five for the third training session. This was after an initial training was performed using previously produced 3D image data from the SAM (Wolny et al., 2020). To estimate performance, images of wild type collected at 3.5 wpg (Fig. 3A) were segmented with boundary prediction models at the different stages of training (Fig. 3C, D). The effect of training iterations was qualitatively and quantitatively evaluated (Fig. 3C-H) by comparison to the respective ground truth.

When comparing the boundary prediction maps before and after training, a sharpening of cell boundary area predictions was observed (Fig. 3C, D). For some cell boundaries, especially in the stem cell area, the model remained uncertain (Fig. 3D, violet zones inside the cells) suggesting that lower staining intensities due to thinner cell walls in this area was more challenging for our model predictions. However, the overall cell area changed only slightly after proofreading of segmentations of wild type, *pxy-2* and *pxy-4* images suggesting that the general prediction was accurate with a slight tendency toward under-segmentation especially for small and weakly stained cells (Fig. 3E).

Further highlighting the positive effect of our training on model accuracy, values for the ‘adapted rand’ decreased significantly already after the first training using the SAM-derived data (Fig. 3F). The ‘adapted rand’ estimates how much the cell segmentation generated by the model fits the ground truth. Adapted rand values remained stable for the rest of the training suggesting that training on hypocotyl sections did not have an added value in this case. This was different for the Variation Of Information\_merge (VOI\_merge) score indicating the degree of undersegmentation (Fig. 3G). VOI\_merge values decreased after the first round of training using the SAM data and dropped even more after the second round of training using images of hypocotyl sections. Also in this case, values remained stable over the remaining training sessions (Fig. 3G). This was again in contrast to the Variation Of Information\_split (VOI\_split) score estimating the degree of oversegmentation. VOI\_split values increased after the first set of hypocotyl images were included, but gradually dropped during the following training sessions (Fig. 3H). Therefore, our training made our model more accurate, with the training by the SAM data having already a profound effect. However, additional rounds of training using hypocotyl images (two rounds using ground truth of corrected segmentations from ten sections each, followed by the last round using ground truth of corrected segmentations from five sections) were important to minimize over- and under-segmentation of the rather noisy and complex data provided. In order to further improve the model performance, we performed a grid search of the training hyperparameters for tuning several combinations of model sizes, training losses, learning rates, and weight regularizations. However, these experiments did not lead to improved segmentations, letting us continue with the model trained with the default parameters (Fig. 3F-H). Importantly, our training reduced the required proofreading time by half compared to the time spent on segmentations generated by default models (e.g. to 2 h for a quarter of a hypocotyl section from 3.5 wpg old plants).

#### 3.3. Cell type classification identifies main cell and tissue types

Next, segmented and raw images were uploaded to MorphographX (MGX) which allows extracting a wide range of morphometric and topological descriptors from segmented objects (cells) and the association

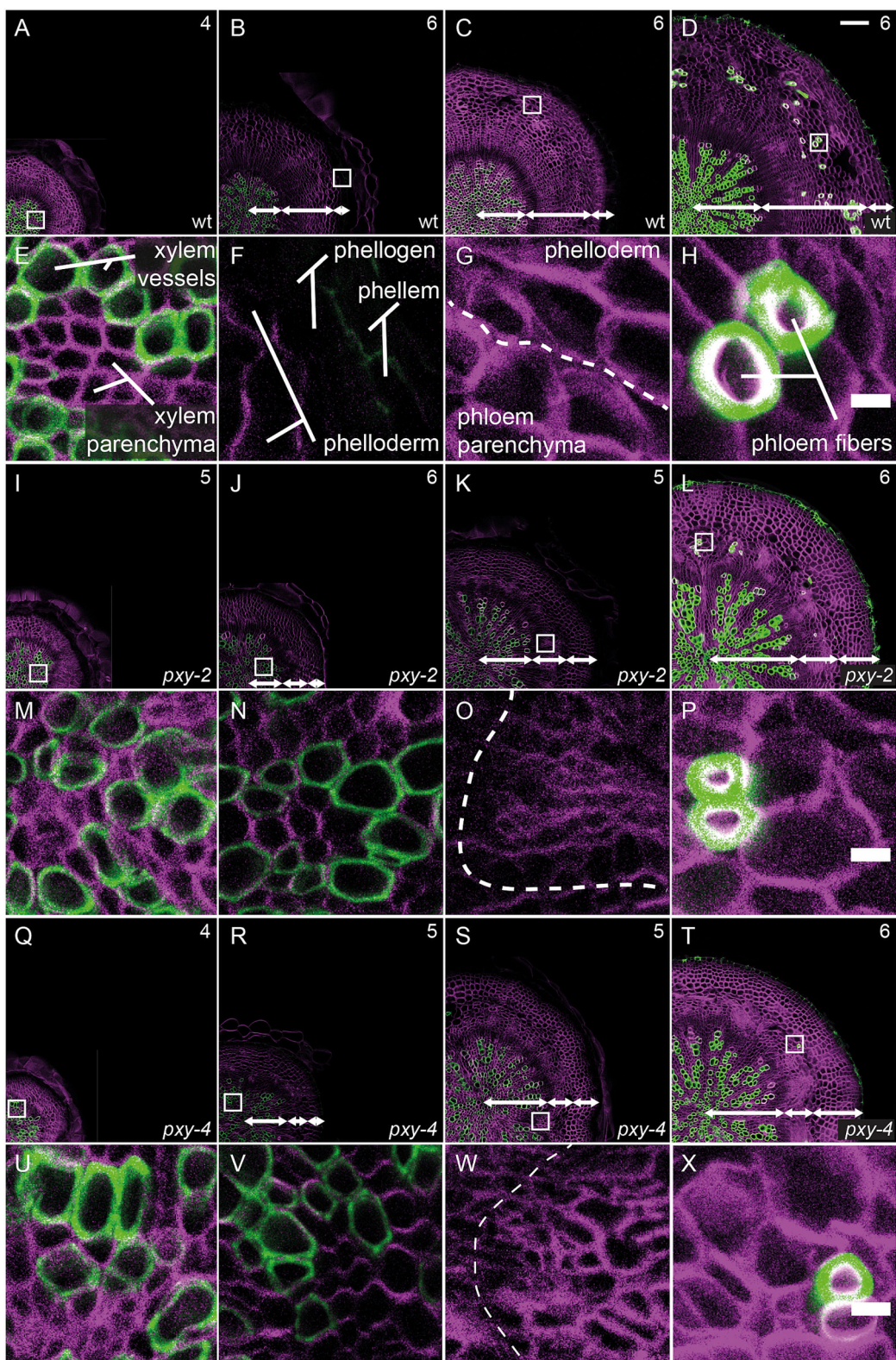


**Fig. 2.** Cell and tissue morphology of the hypocotyl. Sections from hypocotyls harvested at 3.5 wpg (A, E, I, M, Q, U), 4 wpg (B, F, J, N, R, V), 4.5 wpg (C, G, K, O, S, W) and 5 wpg (D, H, L, P, T, X) from wild type (A-H), *pxy-2* mutants (I-P) and *pxy-4* mutants (Q-X) stained with DirectYellow96 (magenta) and Basic Fuchsin (green). In the upper right corner, the number of analyzed plants is indicated. The double-arrows indicate xylem, cambium with phloem and periderm, respectively, from the section center to the periphery. In E-H, M-P, U-X magnifications of the areas indicated by white rectangles shown in A-D, I-L, Q-T, respectively, are shown. (E, M, U) Xylem parenchyma in magenta and xylem vessels in green and white. (F) Periderm with phellogen and phellem in magenta and phellem in green. (G) The identified boundary between the distal phloem and the phellogen (dashed line). (O, W) The cambium contours are indicated by the dashed line showing the break of its radial symmetry in *pxy* mutants. (H, P, X) Mature phloem fibers in green and white. The scale bar in D corresponds to 100  $\mu$ m and applies to A-D, I-L, Q-T, respectively. The scale bar in H, P, X corresponds to 10  $\mu$ m and applies to E-H, M-P, U-X, respectively.

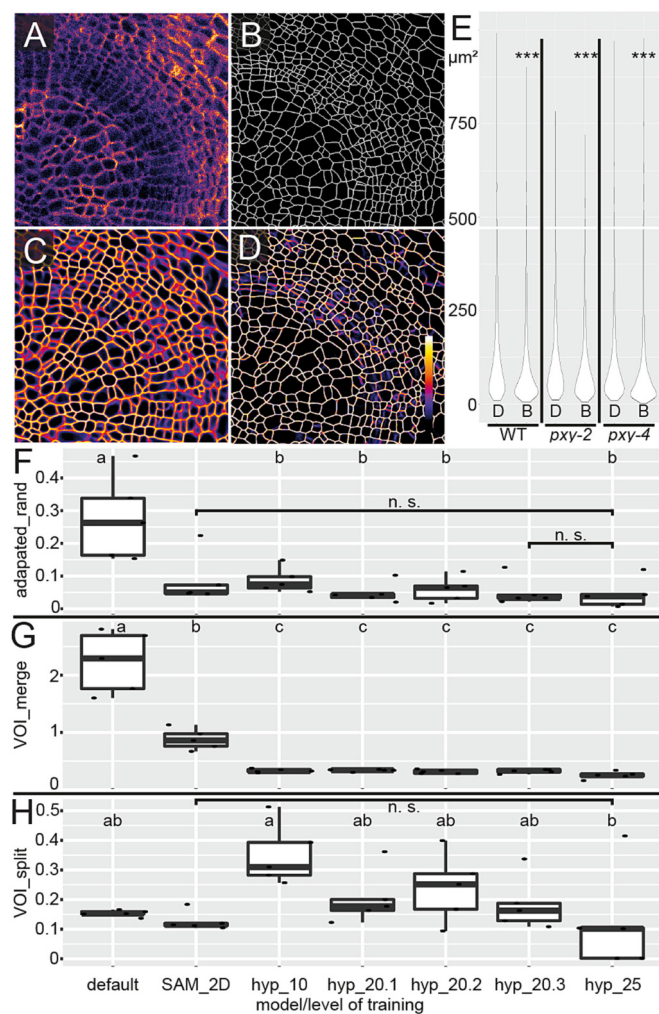


**Fig. 3.** Training of the boundary prediction model. (A) Section of a wild type hypocotyl harvested at 3.5 wpg stained by DirectYellow96. (B) Ground truth of A. (C, D) Boundary prediction maps of A where the highest value (see the calibration bar in D) corresponds to 100 % probability for the pixel to be a cell boundary, while the lowest value corresponds to 0 % of this probability. Boundary prediction map produced by the default PlantSeg model (confocal\_2D\_unet\_bce\_dice.ds2x) is shown in C. Boundary prediction map by the trained model (hyp\_20.3 in F–H) is shown in D. (E) Area of objects (cells) in a quarter of a hypocotyl section of the three indicated genotypes at 5 wpg. D corresponds to the values extracted from a non-proofread segmentation as shown in D. B corresponds to the values extracted from a ground truth as shown in B. (F–H) Segmentation evaluation scores with zero values corresponding to the perfect match of a segmentation from the boundary prediction map to the segmentation from the ground truth. Every model on the x-axis corresponds to stages of training where ‘default’ is the initial default PlantSeg model (confocal\_2D\_unet\_bce\_dice.ds2x), SAM\_2D is the default model trained on SAM data, hyp\_10 is the SAM\_2D model trained on 10 hypocotyl sections, hyp\_20.1 and hyp\_20.2 are hyp\_10 models trained on additional 10 hypocotyl sections with a hyperparameter grid search, hyp\_20.3 is hyp\_10 trained on the same additional 10 hypocotyl sections as hyp\_20.1 and hyp\_20.2 but without the parallelisation, hyp\_25 is hyp\_20.3 trained on another 5 hypocotyl sections. (F) Adapted rand score. (G) Undersegmentation score. (H) oversegmentation scores. Violin plots in E represent the distribution of values. \*\*\* indicate  $p < 0.001$  after pairwise Wilcoxon test between D and B. Boxplots with whiskers in F–H represent standard values. Letters correspond to statistically different groups after one-way ANOVA test and post-hoc pairwise t-test with  $p$ -value  $<0.05$ . Samples without letters showed a non-normal distribution and were compared to hyp\_25 with pairwise Wilcoxon test resulting in non-significant (n.s.) difference ( $p$ -value  $>0.05$ ).

of pixel brightness in original images to these objects (Strauss et al., 2022). In our case, we extracted values for 15 descriptors (see methods section) from each cell which we used for Support Vector Machine (SVM) cell type classification. For every cell type (Fig. 1B), we initially annotated at least 10 cells per cell type on wild type sections. With this selection, an SVM classifier was trained allowing it to attribute cells to the corresponding cell types based on the values of the provided cell descriptors. This approach, together with a manual identification of phloem fibers after the automated classification, allowed the faithful classification of six cell types: xylem vessels, xylem parenchyma, cambium, phloem fibers, phloem parenchyma, and periderm (Fig. S1). When cell type classification was applied to pxy mutants, the ‘cambium’ class was more intermingled with ‘xylem vessel’ and the ‘xylem parenchyma’ classes than in wild type and a “wavier” ‘cambium’ domain was detected (Fig. S2). Moreover, both pxy mutants had produced fewer cells five weeks after germination, which, according to our cell type classification, was caused by a reduction in the number of cambium cell and a reduction of the cell numbers in peripheral tissues (Fig. S2). As these anatomical alterations were described previously (Etchells et al., 2012; Lebovka et al., 2023), we concluded that our trained algorithm faithfully reported biologically relevant anatomies and cell types.

To provide a more visual impression of cell proliferation in both radial and circumferential directions, we transformed the polar tissue representation to a Cartesian one (Fig. 4). This representation clearly visualized the continuous increase in cell numbers in all tissues except, as expected, in the most central xylem. In particular, the Cartesian representation revealed the formation of more dense clusters of cells in the phloem area presumably corresponding to phloem poles, in which additional cell proliferation takes place (Miyashima et al., 2019). A patchier increase of cell numbers was also observed in the cambium domain of pxy mutants (Fig. 4) being in line with a local loss of cambium organization in this background (Lebovka et al., 2023). In addition, the Cartesian display revealed that fewer cells organized in files in the xylem and phloem area of pxy mutants when compared to wild type again demonstrating a more chaotic tissues production in PXY-deficient backgrounds. Therefore, coordinate transformation of hypocotyl cells brought another qualitative perspective on tissue topology during radial hypocotyl growth.

#### 3.4. Mapping of quantitative properties of hypocotyl cells

To get an impression on the distribution of key cell values, we next generated heat maps for selected cell descriptors. Because DirectYellow96 staining was used to identify cell boundaries, we used staining intensity for each segmented cell as an approximation for the degree of cell wall deposition. As expected for differentiated cells, allocation of respective staining intensity to each cell revealed more cell wall deposition in cambium-derived tissues in comparison to cells within the cambium domain (Fig. 5A–D). In pxy mutants, this distribution was disrupted with a more homogenous cell wall staining throughout the section (Fig. 6A–D) suggesting a loss of stem cell attributes in the cambium domain in this background.

A loss of stem cell attributes in PXY-deficient lines was also suggested when analyzing cell area. Cambium cells in pxy mutants were larger than cambium cells in wild type and the clear circular domain harbouring cells with a small area was less pronounced than in wild type (Fig. 5E–H, Fig. 6E–H, Fig. S3C). In wild type, the area of cambium cells remained stable around a value of  $30 \mu\text{m}^2$  over the investigated time points (Fig. 5E–H, Fig. S3C). In comparison, the area of xylem parenchyma cells increased by a factor of 1.5 during the period from 3.5 to 4.5 wpg, the phloem parenchyma cell area gradually doubled until 5 wpg, and the periderm cell area tripled from 3.5 to 4.5 wpg (Fig. 5E–H, Fig. S3B, E, F). Interestingly, the area of newly produced xylem vessels remained constant around a value of  $100 \mu\text{m}^2$  (Fig. 5E–H, Fig. S3A) indicating that the differentiation of vessel elements is rather stable over time.

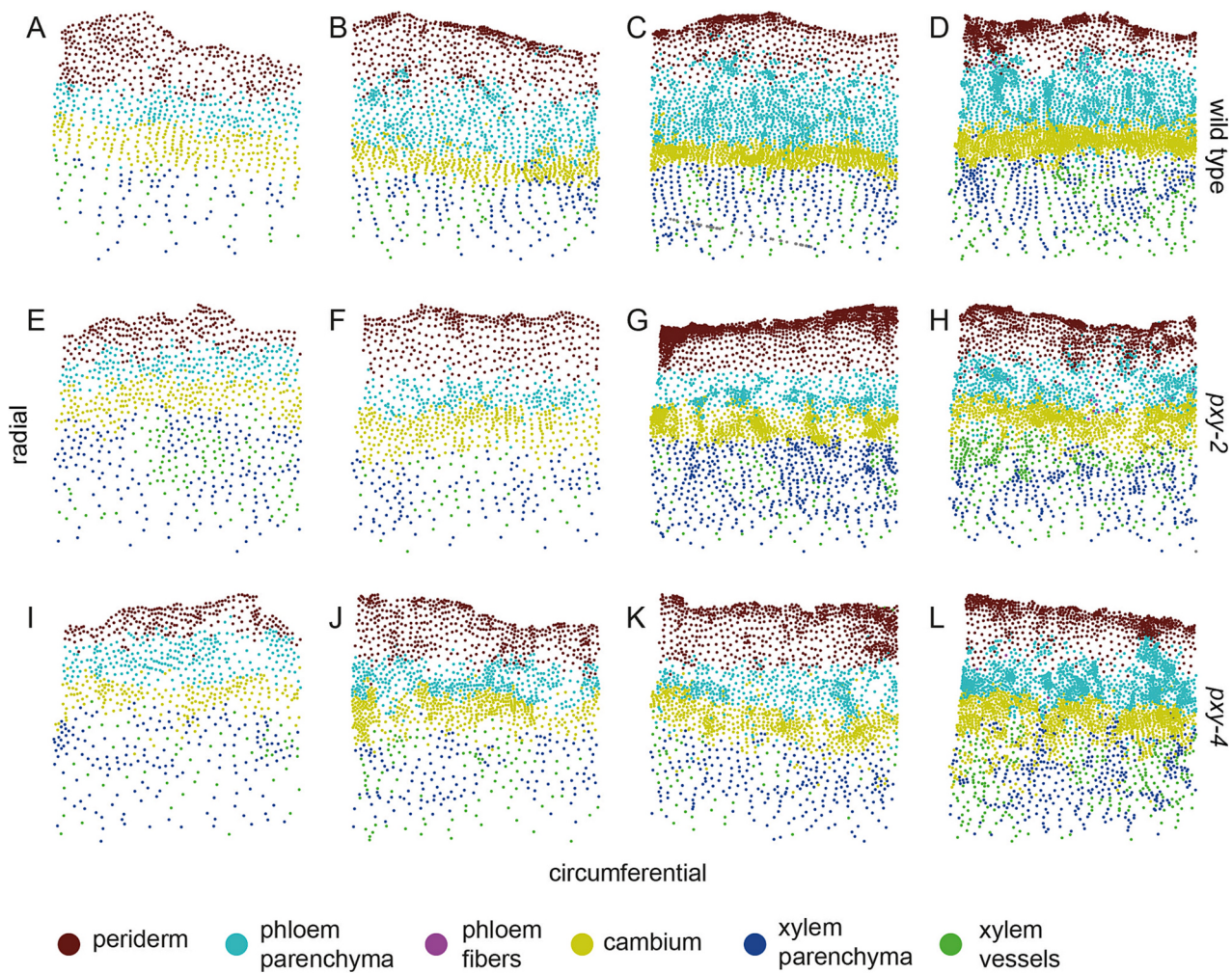


**Fig. 4.** Cell plots from wild type and *pxy* mutant hypocotyls collected at different time points during radial growth. (A-D) wild type. (E-H) *pxy-2*. (I-L) *pxy-4*. (A, E, I) 3.5 wpg. (B, F, J) 4 wpg. (C, G, K) 4.5 wpg. (D, H, L) 5 wpg. Each dot indicates the center of a cell.

Because hypocotyl expansion may lead to a change of cell shape through passive stretching especially in peripheral tissues, we were interested in whether such an effect can be observed by visualizing the spatio-temporal patterns of values indicating cell shape and anisotropy. One informative descriptor in this context is the aspect ratio, the ratio between major and minor axes of a cell and, thus, indicating its degree of anisotropy. In addition, the incline angle, the angle formed between the major axis of the cell and the radial axis of the hypocotyl section crossing the cell centre, indicates how much the major axis of a cell is tilted away from the radial axis of the hypocotyl. If cells were indeed stretched in peripheral hypocotyl tissues, we expected a strong difference in the incline angle comparing central and peripheral tissues.

In the corresponding heat map, the aspect ratio of hypocotyl cells was found to be in a range between 1 and 3 (Fig. 5I-L, Fig. S4). Interestingly, during hypocotyl development, individual cells in all tissues had the tendency to become more anisotropic. This was most pronounced in peripheral tissues like the periderm and the outer phloem area (Fig. 5I-L, Fig. S4) being in line with a prominent growth rate present in this area. In *pxy* mutants, cells followed in general the same trend as in wild type for the aspect ratio over time (Fig. 6I-L, Fig. S4E, F). The exceptions from that trend were some cambium cells which became more anisotropic in *pxy* mutants at later time points in comparison to wild type (Fig. 6I-L, Fig. S4C) again indicating an altered behavior of stem cells in this background. A strong expansion of peripheral cells during organ expansion was further supported by determining their incline angle. Whereas the major axis of central xylem cells mostly

aligned to the radial axis, the major axes of phloem and periderm cells mostly aligned in circumferential orientation (Fig. 5M-P, Fig. S5A, B, D, E, F). The orientation of major cambium cell axes was rather mixed in comparison (Fig. 5M-P, Fig. S5C). Possibly reflecting a reduced growth rate, the incline angle of cells was more homogenous between central and peripheral tissues in *pxy* mutants at early stages but diversified similarly as in wild type at 4.5 and 5 wpg (Fig. 6M-P, Fig. S5).

### 3.5. Investigation of topological features reveals possible paths for lateral movement

Having access to topological features of hypocotyl cells, we next were interested in their betweenness centrality (BC). BC values indicate how often a path may be taken through a distinct cell while “travelling” between all the possible pairs of cells in a given array. Because symplastic transport from cell to cell in lateral orientation is supposed to be an important feature of plant growth axes, determination of BC values may predict paths along which molecules predominantly move. Interestingly, although the BC of most of hypocotyl cells in all genotypes was close to zero, files of cells were identified in which BC values ranged until 0.2 (Fig. 5Q-T, Fig. S6). These files showed a reticulate pattern with prominent tracks in the distal phloem and the periderm where they aligned in circumferential orientation. In addition, files with medium BC values were detected in radial orientation bridging peripheral tissues and the central xylem area. The number radial files with higher BC values was around 2–3 at all growth stages and up to 5–7 for files with

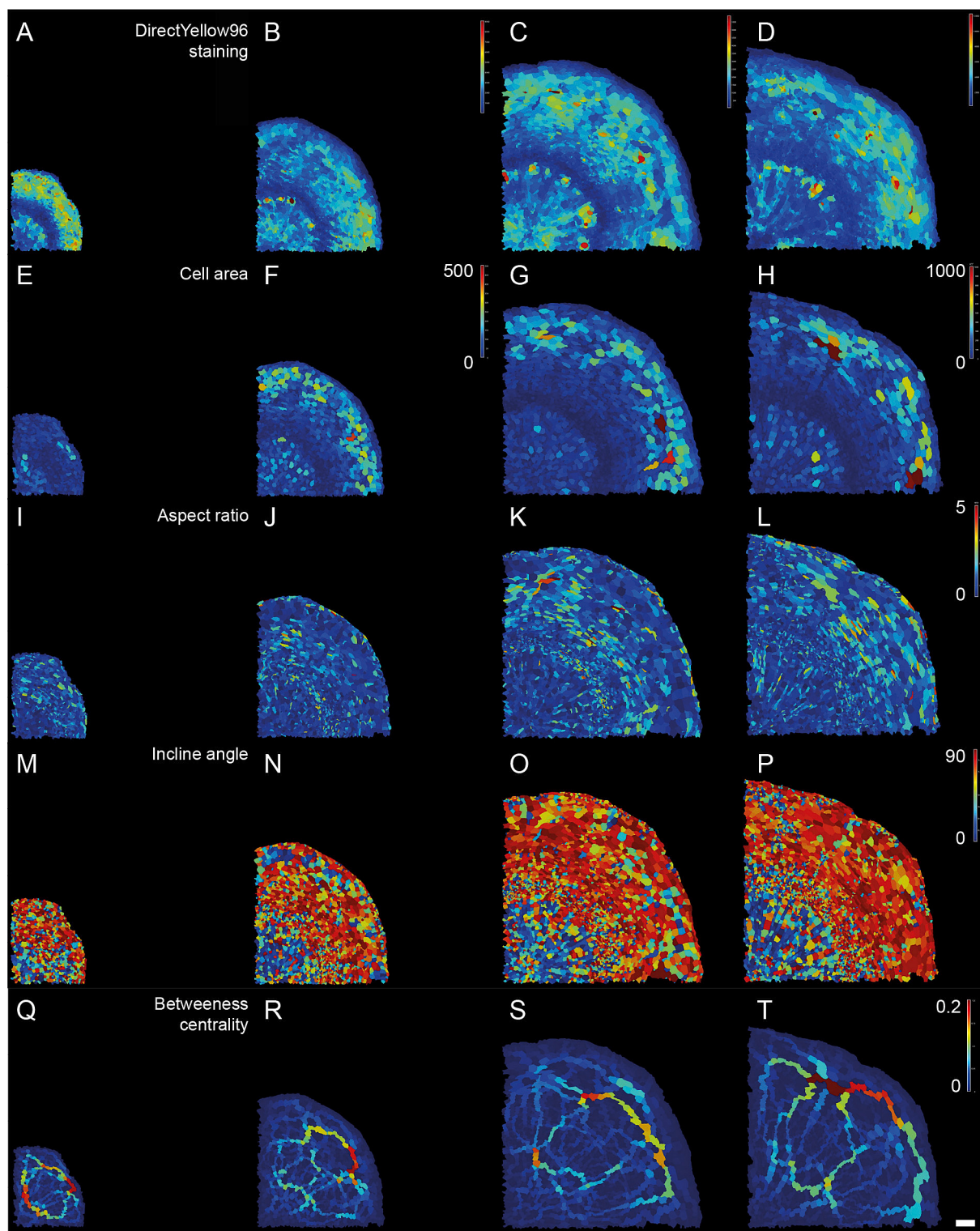


**Fig. 5.** Heatmaps visualizing values of different cell descriptors deduced from wild type. (A-D) Relative DirectYellow96 staining intensities. (E-H) Cell area in  $\mu\text{m}^2$ . (I-L) Aspect ratio. (M-P) Incline angle in  $^\circ$ . (Q-T) Betweenness centrality. (A, E, I, M, Q) 3.5 wpg. (B, F, J, N, R) 4 wpg. (C, G, K, O, S) 4.5 wpg. (D, H, L, P, T) 5 wpg. Color bars on the right indicate values for each row, except the color bar in F applies also to E and the color bar in H applies also to G. Scale bar in T corresponds to 50  $\mu\text{m}$ .

medium values (Fig. 5Q-T). The space between the radial files remained stable over time. In comparison to wild type, *pxy* mutants did not show a striking alteration of their BC value distribution (Fig. 6Q-T, Fig. S6). In summary, determining the spatial pattern of BC values revealed cell files forming circumferential tracks in the phloem area and radial tracks connecting phloem and xylem tissues.

#### 4. Discussion

The focus of this study was the morphometric analysis of radial growth in *Arabidopsis thaliana* at the cellular level and the comparison of different genetic backgrounds. In this context, we established a quantitative histology pipeline based on the PlantSeg and MGX image analysis

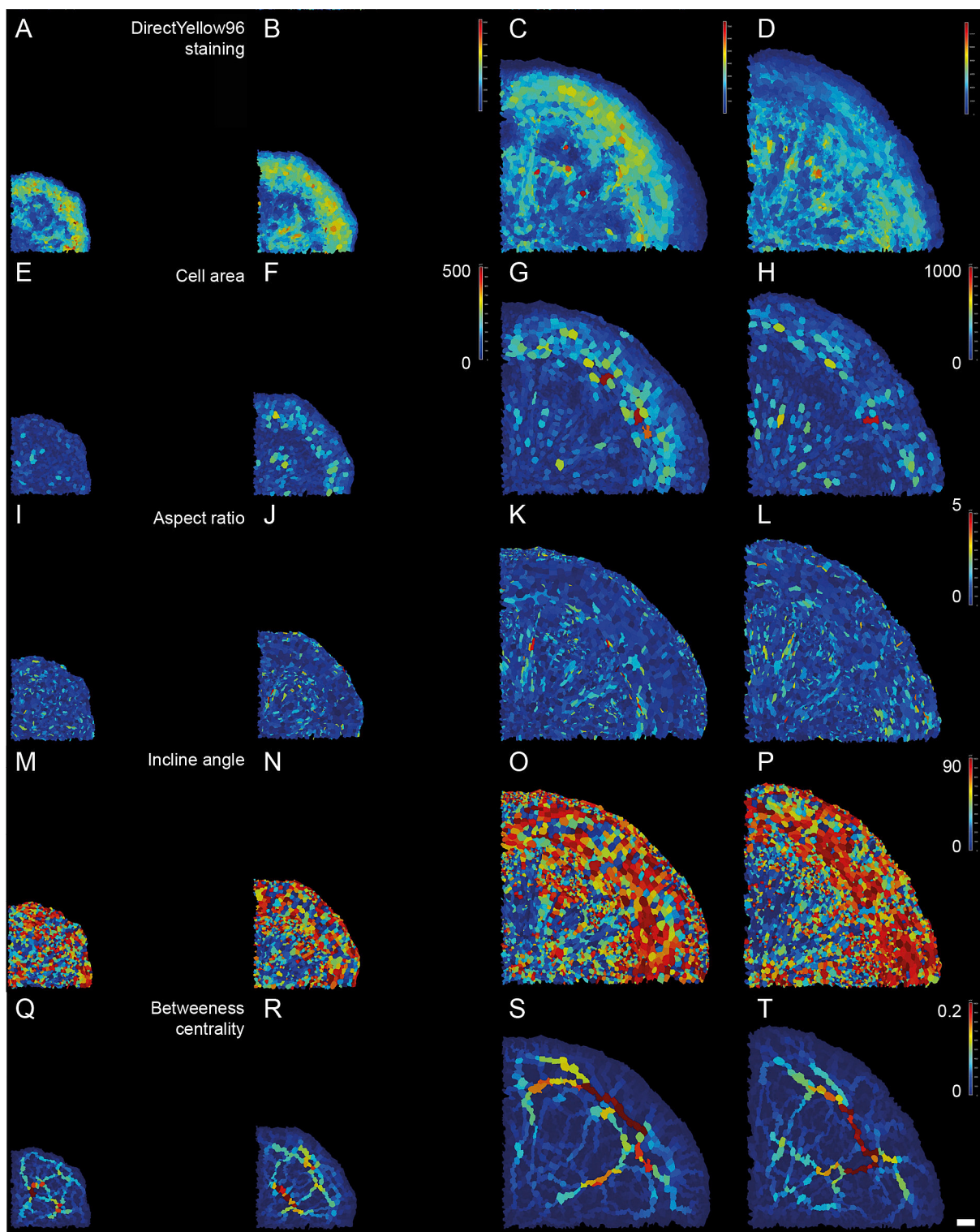


**Fig. 6.** Heatmaps visualizing values of different cell descriptors deduced from *pxy-2*. (A-D) Relative DirectYellow96 staining intensities. (E-H) Cell area in  $\mu\text{m}^2$ . (I-L) Aspect ratio. (M-P) Incline angle in °. (Q-T) Betweenness centrality. (A, E, I, M, Q) 3.5 wpg. (B, F, J, N, R) 4 wpg. (C, G, K, O, S) 4.5 wpg. (D, H, L, P, T) 5 wpg. Color bars on the right indicate values for each row, except the color bar in F applies also to E and the color bar in H applies also to G. Scale bar in T corresponds to 50  $\mu\text{m}$ .

tools. This pipeline allowed us to collect quantitative information on morphological and topological features of growing hypocotyls difficult to collect in such a breadth otherwise.

Automated image analysis including cell type classifications were done on transverse hypocotyl sections before (Bagdassarian et al., 2020; Sankar et al., 2014; Hall et al., 2016). However, until now, multiple

technical limitations related to sample embedding and imaging hindered an efficient and unbiased quantitative histology. In order to preserve cell integrity, hypocotyls were embedded in paraffin (Bagdassarian et al., 2020) or plastic (Sankar et al., 2014) and imaged using bright field microscopy. This did not allow the usage of confocal microscopy combined with the analysis of fluorescent promoter-

reporters. Moreover, cell segmentations from paraffin-embedded samples were done manually probably because of insufficient resolution or cell damages (Bagdassarian et al., 2020). In comparison, plastic embedding better preserve cell integrity (Sankar et al., 2014) but are time-consuming compared to agarose-embedded samples used in the current study. Sankar et al. (Sankar et al., 2014) imaged 144 panels for each section of mature hypocotyls with a resolution  $1024 \times 1024$  pixels each in the bright field mode. In the current study, the same imaging was done with only 9 panels for each section from mature hypocotyls with a resolution  $2048 \times 2048$  pixels and by using confocal imaging. Confocal imaging and cell segmentation of hypocotyl sections was also realized previously. However, no quantitative evaluation of segmentation accuracy was performed, leaving doubts on the correspondence of analyzed labels to actual cell shapes (Hall et al., 2016). In the current study, quantitative evaluation by using novel computational methods like calculating the Adapted Rand and VOI over- and under-segmentation scores (Wolny et al., 2020) was performed suggesting a high accuracy. Moreover the usage of PlantSeg (Wolny et al., 2020) for segmentation instead of the tools used in previous studies like MorphoGraphX (Strauss et al., 2022) or DIPImage (Matlab) (Hall et al., 2016), allowed accessing a broader spectrum of graph-partitioning algorithms. Instead of using classic Watershed algorithms (Hall et al., 2016), we applied MutexWS after testing different algorithms offered by PlantSeg. These algorithms, as well as their parameterisation, can be adjusted to different samples in future quantitative histology studies.

Prior to this study, 3D cell segmentations were performed on young and transparent organs like young hypocotyls (Jackson et al., 2017), root tips (Graeff et al., 2021), or ovules (Wolny et al., 2020) with relatively homogenous cell appearance after clearing and cell wall staining. Although images of hypocotyl sections have only two spatial dimensions, challenges are manifold. In mature hypocotyls, cells are exceptionally heterogeneous with regard to their size and their wall properties. This leads to rather noisy images hampering efficient segmentation. Moreover, the number of cells included in one cross section of a mature hypocotyl is with 10,000–20,000 cells much higher than during previous 3D analyses (Wolny et al., 2020). The CNN used for segmentation in the PlantSeg tool (Wolny et al., 2020) clearly addressed these issues. With limited correction, we were able to extract a multitude of cellular descriptors for several thousands of cells allowing quantitative and statistical analysis of hypocotyl anatomy during radial organ expansion.

Interestingly, our boundary prediction model was trained on images from different organs (ovules, SAM, hypocotyls) and the input from different organs substantially improved the segmentation of hypocotyl images. Thus, boundary prediction models can be exchanged between different organs and boundary prediction benefits from data obtained in other contexts. Obviously, it will be interesting to test how our trained model performs on other organs previously unseen by it. On one hand, a CNN model can only get better by being trained on similar images. On the other hand, our current model may predict boundaries in hypocotyl images that would not be important in another organ. Still, a general segmentation workflow capable of recognising boundaries and shapes in any context comparable to the human eye is one goal of automated image analysis.

Importantly, segmentation was substantially improved after every round of training leading to a reduction of time required for correction after every training iteration. However, the distribution of cell size (area) was different between the segmentations produced by the final boundary prediction model and the ones that we corrected. Still, depending on the purpose and considering the high fraction of cells in a hypocotyl image being correctly segmented, the remaining mistakes might be neglectable during most applications.

As reported previously (Sankar et al., 2014), the incline angle of xylem cells aligned with the radial axis, the major axis of phloem cells aligned with the circumferential one, while the major axis of cambium cells oscillated between both. This is indicative of a circumferential

expansion of peripheral tissues during radial hypocotyl growth. At the very periphery, in the periderm, this expansion is combined with cell divisions preventing tissue disruption (Serra et al., 2022). Exemplarily for other descriptors, the loss of radial patterns of cell descriptors is disturbed in *pxy* mutants and cell type classification identifies altered patterns of cell types in this background. Therefore, our model is able to recognize and quantify mutant phenotypes, a significant tool for an unbiased characterization of different genetic backgrounds. Recently, we modelled *pxy* function in a cell-based approach and postulated the existence of phloem-derived factors in addition to the *pxy* ligand CLE41 promoting stem cell independently from *pxy* (Lebovka et al., 2023). The unequal distribution of those additional factors may be a reason why apparent stem cell loss does not happen thoroughly in *pxy*-deficient plants but is restricted to certain domains resulting in ‘wavy’ pattern of the cambium domain.

By determining the betweenness centrality (BC) we identified “cell roads” oriented circumferentially in the phloem and radially crossing the cambium area. Because sugars most likely move from transporting sieve elements in the phloem circumferentially and toward the cambium and the xylem radially, it will be interesting to see whether this topological feature identified here, holds biological relevance. Future experiments with fluorescent dyes travelling from phloem or xylem toward other tissues may elucidate if such roads indeed exist.

## 5. Conclusion

Our study aimed to describe cell and tissue morphogenesis in the context of radial plant growth. A quantitative histology protocol was established and used on different genotypes and different growth stages. Using this protocol, the phenotype of mutants affected in various radial growth-related parameters can be characterized in a non-biased, quantitative way allowing the assignment of morphogenic functions to underlying genes. Moreover, feeding collected data into computational models simulating molecular, chemical or mechanical properties (Lebovka et al., 2023) will allow simulations using realistic anatomies.

Supplementary data to this article can be found online at <https://doi.org/10.1016/j.cdev.2023.203842>.

## CRediT authorship contribution statement

AZ performed most of the experiments, created the figures, and wrote a draft of the manuscript. LC provided central support in image analysis, model training and in using the PlantSeg application. TG was involved in the study design and its supervision, and wrote the final version of the manuscript.

## Declaration of competing interest

The authors declare no conflict of interest.

## Data availability

Data will be made available on request.

## Acknowledgements

This work was supported by the Deutsche Forschungsgemeinschaft (DFG) through the Research Unit FOR 2581 ‘Quantitative Morphodynamics of Plants’ and the SFB 873 ‘Maintenance and Differentiation of Stem Cells in Development and Disease’ (grant INST 35/1305). We thank Richard Smith (JIC, Norwich, UK) and Sören Strauss (MPIPZ, Cologne, Germany) for support in MGX.

## References

- Bagdassarian, K.S., Connor, K.A., Jermyn, I.H., Etchells, J.P., 2020. Versatile method for quantifying and analyzing morphological differences in experimentally obtained images. *Epub 2019/11/26 Plant Signal. Behavior* 15 (1), 1693092. <https://doi.org/10.1080/15592324.2019.1693092>. PubMed PMID: 31762388; PubMed Central PMCID: PMC7012139.
- Berg, S., Kutra, D., Kroeger, T., Straehle, C.N., Kausler, B.X., Haubold, C., et al., 2019. ilastik: interactive machine learning for (bio)image analysis. *Epub 2019/10/02 Nat. Methods* 16 (12), 1226–1232. <https://doi.org/10.1038/s41592-019-0582-9>. PubMed PMID: 31570887.
- Etchells, J.P., Provost, C.M., Turner, S.R., 2012. Plant vascular cell division is maintained by an interaction between PXY and ethylene signalling. *PLoS Genetics* 8 (11), e1002997. *Epub 2012/11/21*. PubMed PMID: 23166504; PubMed Central PMCID: PMC3499249.
- Fisher, K., Turner, S., 2007. PXY, a receptor-like kinase essential for maintaining polarity during plant vascular-tissue development. *Curr. Biol.* 17 (12), 1061–1066. PubMed PMID: 17570668.
- Graeff, M., Rana, S., Wendrich, J.R., Dorier, J., Eekhout, T., Aliaga Fandino, A.C., et al., 2021. A single-cell morpho-transcriptomic map of brassinosteroid action in the Arabidopsis root. *Epub 2021/08/07 Molecular Plant* 14 (12), 1985–1999. <https://doi.org/10.1016/j.molp.2021.07.021>. PubMed PMID: 34358681; PubMed Central PMCID: PMC8674818.
- Greb, T., Lohmann, J.U., 2016. Plant stem cells. *Curr. Biol.* 26 (17), R816–R821. *Epub 2016/09/14* PubMed PMID: 27623267.
- Haas, A.S., Shi, D., Greb, T., 2022. Cell fate decisions within the vascular cambium-initiating wood and bast formation. *Epub 2022/05/14 Front Plant Sci.* 13, 864422. <https://doi.org/10.3389/fpls.2022.864422>. PubMed PMID: 35548289; PubMed Central PMCID: PMC9082745.
- Hall, H.C., Fakhrzadeh, A., Luengo Hendriks, C.L., Fischer, U., 2016. Precision automation of cell type classification and sub-cellular fluorescence quantification from laser scanning confocal images. *Epub 2016/02/24 Front Plant Sci.* 7, 119. <https://doi.org/10.3389/fpls.2016.00119>. PubMed PMID: 26904081; PubMed Central PMCID: PMC4746258.
- Jackson, M.D., Xu, H., Duran-Nebreda, S., Stamm, P., Bassel, G.W., 2017. Topological analysis of multicellular complexity in the plant hypocotyl. *Epub 2017/07/07 elife 6*. <https://doi.org/10.7554/elife.26023>. PubMed PMID: 28682235; PubMed Central PMCID: PMC5499946.
- Lebovka, I., Hay Mele, B., Zakieva, A., Schlamp, T., Gursanscky, N., Merks, R.M.H., et al., 2023. Computational modelling of cambium activity provides a regulatory framework for simulating radial plant growth. *elife* 12, e66627. <https://doi.org/10.7554/elife.66627>.
- Lehmann, F., Hardtke, C.S., 2016. Secondary growth of the *Arabidopsis* hypocotyl-vascular development in 4 dimensions. *Epub 2015/12/17 Curr Opin Plant Biol.* 29, 9–15. <https://doi.org/10.1016/j.pbi.2015.10.011>. PubMed PMID: 26667498.
- Miyashima, S., Roszak, P., Sevilem, I., Toyokura, K., Blob, B., Heo, J., et al., 2019. Mobile PEAR transcription factors integrate hormone and miRNA cues to prime cambial growth. *Nature* 565 (7740), 490–494. <https://doi.org/10.1038/s41586-018-0839-y>.
- Montenegro-Johnson, T., Strauss, S., Jackson, M.D.B., Walker, L., Smith, R.S., Bassel, G. W., 2019. 3DCellAtlas Meristem: a tool for the global cellular annotation of shoot apical meristems. *Epub 2019/04/17 Plant Methods* 15, 33. <https://doi.org/10.1186/s13007-019-0413-0>. PubMed PMID: 30988692; PubMed Central PMCID: PMC6448224.
- Sankar, M., Nieminen, K., Ragni, L., Xenarios, I., Hardtke, C.S., 2014. Automated quantitative histology reveals vascular morphodynamics during *Arabidopsis* hypocotyl secondary growth. *Epub 2014/02/13 elife* 3, e01567. <https://doi.org/10.7554/elife.01567>. PubMed PMID: 24520159; PubMed Central PMCID: PMC3917233.
- Apala, A., Runions, A., Routier-Kierzkowska, A.L., Das Gupta, M., Hong, L., Hofhuis, H., et al., 2018. Why plants make puzzle cells, and how their shape emerges. *Epub 2018/02/28 elife* 7. <https://doi.org/10.7554/elife.32794>. PubMed PMID: 29482719; PubMed Central PMCID: PMC5841943.
- Schindelin, J., Arganda-Carreras, I., Frise, E., Kaynig, V., Longair, M., Pietzsch, T., et al., 2012. Fiji: an open-source platform for biological-image analysis. *Nature Methods* 9 (7), 676–682. *Epub 2012/06/30*. PubMed PMID: 22743772; PubMed Central PMCID: PMC3855844.
- Serra, O., Mähönen, A.P., Hetherington, A.J., Ragni, L., 2022. The making of plant armor: the periderm. *Epub 2022/01/06 Annu. Rev. Plant Biology.* 73, 405–432. <https://doi.org/10.1146/annurev-aplant-102720-031405>. PubMed PMID: 34985930.
- Spicer, R., Groover, A., 2010. Evolution of development of vascular cambia and secondary growth. *New Phytol.* 186 (3), 577–592. <https://doi.org/10.1111/j.1469-8137.2010.03236.x>. PubMed PMID: 20522166.
- Strauss, S., Runions, A., Lane, B., Eschweiler, D., Bajpai, N., Trozzi, N., et al., 2022. Using positional information to provide context for biological image analysis with MorphoGraphX 2.0. *Epub 2022/05/06 elife* 11. <https://doi.org/10.7554/elife.72601>. PubMed PMID: 35510843; PubMed Central PMCID: PMC9159754.
- Ursache, R., Andersen, T.G., Marhavy, P., Geldner, N., 2018. A protocol for combining fluorescent protein with histological stains for diverse cell wall components. *Plant J.* 93 (2), 399–412. <https://doi.org/10.1111/pj.13784>. PubMed PMID: 29171896.
- Wolny, A., Cerrone, L., Vijayan, A., Tofanelli, R., Barro, A.V., Louveaux, M., et al., 2020. Accurate and versatile 3D segmentation of plant tissues at cellular resolution. *Epub 2020/07/30 elife* 9. <https://doi.org/10.7554/elife.57613>. PubMed PMID: 32723478; PubMed Central PMCID: PMC7447435.
- Wunderling, A., Ben Targem, M., Barbier de Reuille, P., Ragni, L., 2017. Novel tools for quantifying secondary growth. *Epub 2016/12/15 J. Exp. Botany* 68 (1), 89–95. <https://doi.org/10.1093/jxb/erw450>. PubMed PMID: 27965365.
- Wunderling, A., Ripper, D., Barra-Jimenez, A., Mahn, S., Sajak, K., Targem, M.B., et al., 2018. A molecular framework to study periderm formation in *Arabidopsis*. *Epub 2018/04/04 New Phytol.* 219 (1), 216–229. <https://doi.org/10.1111/nph.15128>. PubMed PMID: 29611875.